Biomaterials Science

ROYAL SOCIETY OF CHEMISTRY

PAPER

View Article Online
View Journal | View Issue

Cite this: *Biomater. Sci.*, 2022, **10**, 138

Characterisation of bone regeneration in 3D printed ductile PCL/PEG/hydroxyapatite scaffolds with high ceramic microparticle concentrations†

Chuanliang Cao,[a] Pengren Huang,[b] Aruna Prasopthum, ‡[c] Andrew J. Parsons,[d] Fanrong Ai*[a] and Jing Yang *[c]

3D printed bioactive glass or bioceramic particle reinforced composite scaffolds for bone tissue engineering currently suffer from low particle concentration (<50 wt%) hence low osteoconductivity. Meanwhile, composites with very high inorganic particle concentrations are very brittle. Scaffolds combining high particle content and ductility are urgently required for bone tissue engineering. Herein, 3D printed PCL/hydroxyapatite (HA) scaffolds with high ceramic concentration (up to 90 wt%) are made ductile (>100% breaking strain) by adding poly(ethylene glycol) which is biocompatible and FDA approved. The scaffolds require no post-printing washing to remove hazardous components. More exposure of HA microparticles on strut surfaces is enabled by incorporating higher HA concentrations. Compared to scaffolds with 72 wt% HA, scaffolds with higher HA content (90 wt%) enhance matrix formation but not new bone volume after 12 weeks implantation in rat calvarial defects. Histological analyses demonstrate that bone regeneration within the 3D printed scaffolds is *via* intramembranous ossification and starts in the central region of pores. Fibrous tissue that resembles non-union tissue within bone fractures is formed within pores that do not have new bone. The amount of blood vessels is similar between scaffolds with mainly fibrous tissue and those with more bone tissue, suggesting vascularization is not a deciding factor for determining the type of tissues regenerated within the pores of 3D printed scaffolds. Multinucleated immune cells are commonly present in all scaffolds surrounding the struts, suggesting a role of managing inflammation in bone regeneration within 3D printed scaffolds.

Received 27th October 2021,
Accepted 12th November 2021

DOI: 10.1039/d1bm01645h

rsc.li/biomaterials-science

1. Introduction

3D printing is a promising manufacturing tool for fabricating scaffolds for bone tissue engineering.[1–4] It offers the ability to precisely control geometry[5,6] and to fabricate stratified structures to mimic the heterogeneity of bone.[7] Various materials including bioceramics,[8,9] bioactive glasses,[10] and biodegradable polymers[11] have been used in 3D printing to produce degradable bone tissue engineering scaffolds. These materials have a good track record of safety, hence, from a regulatory point of view, it is relatively easier to translate 3D printed scaffolds made of them into the clinic. Whilst ceramic and bioactive glass scaffolds offer relatively high modulus, strength and osteoconductivity,[12] their brittleness is a significant concern for clinical applications.[13] Bioceramics and bioactive glasses are intrinsically brittle. They are very sensitive to the presence of small cracks commonly present in porous scaffolds, and can fail catastrophically when subjected to *in vivo* forces. The ductility of bone scaffolds is critical for their mechanical reliability. However, this mechanical property has received less attention compared to modulus and strength. On the other hand, although polymers such as biodegradable polyesters are relatively ductile, they are usually hydrophobic and have poor osteoconductivity and mechanical properties inferior to cortical bone.[14,15]

To overcome limitations associated with single materials, polymer/inorganic composites that mimic, to some extent, bone (which consists of mainly partially carbonated hydroxyapatite and type I collagen fibrils) have been used in 3D printing to combine the ductility of polymers and the osteoconductivity of the inorganic components.[1,11,16,17] A balance between mechanical properties and osteoconductivity needs to be

[a]*School of Mechatronic Engineering, Nanchang University, Nanchang, Jiangxi, China 330031. E-mail: aifanrong@ncu.edu.cn*
[b]*Department of Orthopedic Surgery, The Second Affiliated Hospital of Nanchang University, Nanchang, Jiangxi, China 330006*
[c]*Biodiscovery Institute, University of Nottingham, Nottingham, UK NG7 2RD. E-mail: jing.yang@nottingham.ac.uk*
[d]*Composites Research Group, Faculty of Engineering, University of Nottingham, Nottingham, UK NG7 2RD*
†Electronic supplementary information (ESI) available. See DOI: 10.1039/d1bm01645h
‡Current address: School of Pharmacy, Walailak University, Nakhon Si Thammarat, Thailand, 80160

struck for these composites. Modulus and strength initially increase with the concentration of the inorganic component, subsequently start to plateau before becoming detrimental to the mechanical properties at very high concentrations.[18] Addition of glass or ceramic microparticles into polymers can even lower strength and increase brittleness of composites at very low particle concentrations. For example, in a study in which the mechanical properties of β-tricalcium phosphate/PCL composites were tested, modulus of the composites increased with higher concentrations of the calcium phosphate particles up to 60 wt%. However, the yield strengths of all the composites (20 wt% to 60 wt%) were lower than pure PCL.[19] These studies have demonstrated that although high concentrations of glass/ceramic particles can increase modulus, they can also make the composites more brittle with low strength. As a consequence, the inorganic component is typically kept at relatively low concentration (<50 wt%).[20] On the other hand, higher concentration of the inorganic component is desirable to increase osteoconductivity.[21] Low concentration of the inorganic component in the composites leads to less exposure of them on the surface, which compromises their osteoconductivity as most of them are embedded in the polymer matrix hence not in contact with cells. The osteoconductive properties of bioactive glasses with certain compositions and some calcium phosphates have long been documented. Some studies even showed osteoinductive properties of these materials, although conflicting data on this exist in the literature.[22] The formation of carbonate hydroxyapatite on the material surfaces as well as released ions due to dissolution have been demonstrated to be key for their good osteogenic properties.[23] It is reasonable to postulate that if the glass or ceramic particles are not present on the strut surface of 3D printed scaffolds, their osteoconductive/osteoinductive properties will be compromised. Only few efforts have been made to make composites with high-concentration inorganic component more flexible in which 3D printed scaffolds with high-concentration hydroxyapatite (HA) micro particles (up to 90 wt%) were made elastic and ductile by adding a surfactant (2-butoxyethanol) and a plasticizer (Dibutyl phthalate).[24] However, the inclusion of these additives may have implications in safety and regulation.[25]

Bone regenerates either *via* intramembranous ossification or by endochondral ossification.[26] Intramembranous ossification, which is responsible for the formation of most flat bones, involves the differentiation of mesenchymal cells to osteoblasts, the formation of ossification centres and initial synthesis of collagen fibrils followed by polarized secretion of bone matrix.[27] In endochondral ossification, which is responsible for the formation of long bones, cartilage forms first before being replaced by bone.[28] Bone regeneration *via* endochondral ossification has been considered to be advantageous for biomaterial scaffolds supplemented with stem/progenitor cells due to the requirement of initial vascularization that is critical for cell survival.[29–31] It will be useful to characterise the route of bone formation for the analysis of *in vivo* bone regeneration within 3D printed scaffolds.

Herein, 3D printed PCL/PEG/HA composites with high concentrations (up to 90 wt%) of HA particles were rendered ductile by adding poly(ethylene glycol) (PEG). PEG is an FDA-approved biomaterial that has shown good biocompatibility.[32,33] The optimal molecular weight and concentration of PEG added to the 3D printing ink formulation were identified for achieving ductility. The mechanical properties of individual struts and scaffolds with different HA concentrations were measured. Bone formation within the 3D printed scaffolds were tested *in vivo* using a rat calvarial model. These 3D printed scaffolds are potentially applicable to clinical applications that require ductile and surgically trimmable materials.

2. Materials and methods

2.1 Strut and scaffold fabrication

Polycaprolactone (PCL, M_n = 80 000 g mol^{-1}), poly(ethylene glycol) (PEG, M_n = 400, 3350, 20 000 Da) and hydroxyapatite microparticles (product number 289396) were all purchased from Sigma-Aldrich (UK). The size distribution of the hydroxyapatite microparticles is shown in Fig. S1.† Various formulations of PCL/PEG/HA were made by first dissolving PEG in dichloromethane (DCM), then adding HA microparticles and vortexed until homogeneous, lastly adding PCL and agitating the mixture on a roller overnight. All struts and scaffolds were made using a pneumatic extrusion-based 3D printer (RegenHU, Switzerland) at room temperature in air using a conical needle with a nozzle diameter of 260 μm. The individual struts were extruded at a pressure of 4 bar and then collected in a tray 10–15 cm below the needle. Scaffolds were fabricated by extrusion-based 3D printing using a pressure of 4–6 bar and a printing speed of 12–20 mm s^{-1}. After the printing process, all the individual struts and scaffolds were dried in air for 24 hours at room temperature to eliminate the residual solvent (DCM).

2.2 Mechanical property testing

Single strut tensile testing was performed using a sensitive tensile test facility (LEX810, Diastron Ltd, UK) (Fig. S2†). Struts were fixed individually onto the plastic tabs with a 10 mm gauge length setup. Prior to testing, the diameters of the fibres were measured using an optical microscope. And the samples were stretched to 400% strain at a crosshead speed of 0.04 mm s^{-1} at room temperature in air. Compression testing of scaffolds was performed using a universal texture analyser (TA-HD Plus, Stable Microsystems, USA). The scaffolds (24 layers), with dimensions of 8 (width) × 8 (width) × 4.3 (height) mm^3, were compressed in the height direction with a speed of 0.03 mm s^{-1} to the strain of 60%. The compressive modulus was calculated from the initial linear range of the stress–strain curves (strain range 1% to 5%). At least three specimens were tested for each sample group. Tensile testing was carried out using a universal testing machine with a 10 kN load cell (CMT6104, Mets Industrial Systems Co., Ltd) at a rate of

0.17 mm s^{-1}. Scaffolds (6 layers) used in the tensile testing had dimensions of 20 × 10 × 1 mm^3.

2.3 Scanning electron microscope (SEM)

SEM images were obtained by using a JSM-6490 scanning electron microscope (JEOL, UK). Scaffold samples were mounted on stubs and sputter coated with gold/palladium before imaging. For cell-laden scaffolds, the specimens were fixed in 2.5% (v/v) glutaraldehyde/PBS and stained with 1%(v/v) osmium tetroxide prior to dehydration.

2.4 *In vitro* cell culture

The human mesenchymal stem cells (hMSCs) (TCS Cellworks, UK) were immortalised according to a previous protocol.[34] The cells were expanded in Dulbecco's modified Eagle's (DMEM) medium with 10% (v/v) FBS, 1% (v/v) L-glutamine, 1% (v/v) 1% (v/v) antibiotic/antimycotic (AB/AM) solution and 1% (v/v) non-essential amino acids. The scaffolds were sterilised in 70% (v/v) ethanol for 1 hour, washed with PBS and incubated in DMEM medium containing 10% (v/v) FBS before cell seeding. 1×10^6 cells were seeded into each 3D printed PCL/HA scaffold (1 × 1 × 0.5 cm^3). The osteogenic differentiation medium (αMEM with 10% (v/v) FBS, 1% (v/v) L-glutamine and 1% (v/v) antibiotic/antimycotic solution, 10 mM β-glycerophosphate, 100 nM dexamethasone) was then added after initial attachment of cells to the scaffolds. The hMSC-seeded scaffolds were cultured for 21 days during which the osteogenic differentiation medium was changed twice a week.

hMSC-seeded scaffolds that were cultured in the osteogenic differentiation medium were harvested at different days (day 1, day 7, day 14, and day 21). They were individually washed with ice-cold PBS, homogenised in a lysis buffer containing the Halt™ protease inhibitor cocktail (Thermo Fisher Scientific, UK), and freeze-thawed for three cycles to promote cell lysis. The clear supernatants were then used to measure the quantity of DNA and osteocalcin (a late marker of osteogenesis) using PicoGreen™ and an enzyme-linked immunosorbent assay kit (Thermo Fisher Scientific, UK), respectively. All samples and standards were performed in triplicate. The cell-free scaffolds were used as negative controls.

2.5 *In vivo* testing of scaffolds in rat calvarial defects

The rat calvarial defect model was established on six 8-week old male Spraguee Dawley rats provided by Jiangxi University of Traditional Chinese Medicine (Nanchang, China). Each rat weighted approximately 200 g. All animal procedures were performed in accordance with the guidelines for care and use of laboratory animals of Nanchang University and approved by the Animal Ethics Committee of the Second Affiliated Hospital of Nanchang University. Briefly, the rats were anesthetized with 10% chloral hydrate (4 ml kg^{-1}), and the skin of the surgical site was shaved. The rats were fixed on the operating table and iodophor was used to disinfect the skin of the surgical site. A longitudinal incision about 3 cm long was made along the sagittal line of the skull to expose the skull. Two calvarial defects with a diameter of 5 mm were drilled on both sides of parietal bone with a surgical trephine (Fig. S3†). Rat calvarial defects with 5 mm diameter have been widely used as a bone regeneration model though it may not be considered as critical-sized defects.[35,36] 5 mm defect size allowed the introduction of two defects per rat and the avoidance of the sagittal suture spanning the defect. The operation site was continuously rinsed with saline to reduce heat during drilling. Two different scaffold groups (72% HA and 90% HA) were sterilized by ethylene oxide before being implanted into the defect sites. Six samples were used for each group of scaffolds and two different scaffolds were implanted in a rat. Incisions were then sutured. After waking up, the rats were moved into a clean animal room. All the experimental animals were in good condition and no wound infection was identified. The scaffolds used for implantation were 5 mm in diameter and were punched out from printed scaffolds (mean pore size – 380 μm, strut diameter – 280 μm, porosity – 67% (pores between struts) and 7 layers).

2.6 Gross morphology and micro-CT

After 12 weeks, the animals were sacrificed under general anesthesia, and the specimens were retrieved with some surrounding host bone and fixed with 10% formalin. Gross morphology images were taken using an optical microscope (A005+, Shenzhen SuperEye Technology, China). The fixed specimens were scanned with custom made Micro-CT (Xidian University, Shaanxi, China) with a tube voltage of 78 kV and a tube current of 100 μA. After scanning, a software for isosurface rendering (3D Med 5.0, Chinese Academy of Sciences) was used for 3D reconstruction to evaluate the degree of mineralization.

2.7 Histological analysis

Following Micro-CT analysis, the scaffolds were decalcified in 0.5 M EDTA decalcifying solution for 30 days with frequent changing of the solution every 2–3 days. The specimens were then embedded in paraffin blocks, and transversal slices with 4 μm thickness were cut from the middle of each defect using a microtome. The slices were then washed in xylene to remove paraffin followed by rehydration in ethanol series and water before being stained with hematoxylin and eosin (H&E). For immunohistochemistry, the slices were firstly dewaxed in the same way as those used for H&E staining. They were then incubated in 3% hydrogen peroxide solution followed by 3% bovine serum albumin to block endogenous peroxidase and non-specific binding, respectively, before being incubated with primary anti-Collagen II or anti-osteocalcin (OCN) antibodies. The slices were then washed and incubated in secondary antibodies tagged with horseradish peroxidase followed by being stained in 3,3′-diaminobenzidine chromogenic solution to produce a brown colour where collagen II or OCN was present. All reagents used for histology were from Wuhan Servicebio Technology, China. All images were obtained by an optical microscope (NIKON Eclipse Ci, Japan). Eosin-stained area was measured by using the colour deconvolution function in ImageJ with the same threshold range for all images (National

Institutes of Health, USA). The quantification of collagen II and OCN area was carried out using the IHC plugin in ImageJ as described before.[37]

2.8 Statistical analysis

All data were presented as mean ± standard deviation (SD). Statistical analysis was performed on GraphPad Prism 5 software (Minitab Inc., State College, PA, USA) using one-way analysis of variance (ANOVA) to test for significance. *Post hoc* Tukey's multiple-comparison test was used to determine the individual differences among the groups. Unpaired T test was used when there were only two groups compared.

3. Results

3.1 Effects of PEG concentration and molecular weight on the mechanical properties of struts and scaffolds

Fig. 1 shows two 3D printed structures with a high HA : PCL mass ratio (9 : 1). PEG400 was added to the PCL/HA blend to render ductility. The printed sheet (4 layers) was foldable whilst counterparts without PEG fractured easily after slight bending (Fig. 1a, Fig. S4†). A movie of the folding and unfolding process can be found in Movie S1.† Thicker structures were also printable with satisfactory fidelity (Fig. 1b).

To identify the optimal PEG concentration and molecular weight that were used in the structures shown in Fig. 1 for improving ductility, PEGs with different molecular weights (400, 3350, 20 000 Da) were added to PCL/HA at different concentrations. Individual struts that were made of these materials were measured for their tensile properties. The tensile properties were measured both before and after soaking in water (24 hours) as PEG is hydrophilic and leaches out in aqueous environments. The struts that were soaked in water were dried in air for at least 24 hours before tensile testing. Representative stress–strain curves are shown in Fig. S5.†

Fig. 2 shows the breaking strains of PCL/PEG/HA composite struts with different concentrations and different molecular weights of PEG. For PEG20000 and PEG3350, when the mass ratio of PEG : PCL was below 10 : 10, the struts demonstrated a brittle characteristic, similar to PCL/HA without PEG, before and after immersion. When the mass ratio of PEG : PCL reached 10 : 10, the struts were still relatively brittle. However, the ductility increased dramatically after immersion. The breaking strains increased from 6.2% and 12.1% to 47.9% and 190.5% for the PEG(3350) and PEG(20k) containing struts,

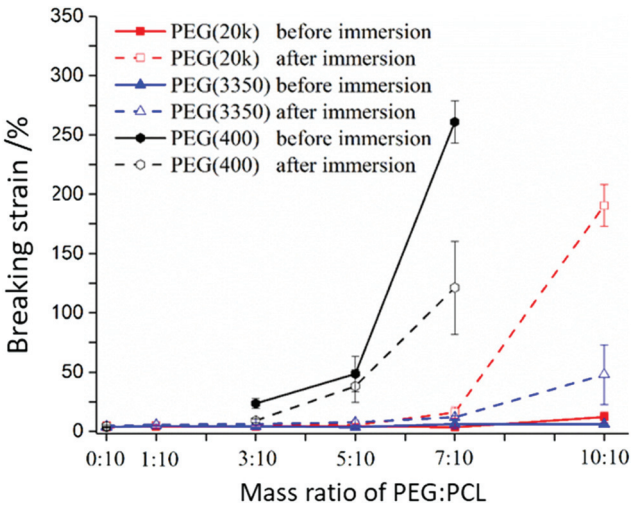

Fig. 2 Tensile breaking strain of PCL/PEG/HA struts. The PCL : HA mass ratio was fixed at 1 : 9. Struts were tested in air. Immersion means that struts were soaked in water for 24 hours and then dried in air before testing. Data represent mean ± SD, n = 5. Lines are used only for guiding the eyes.

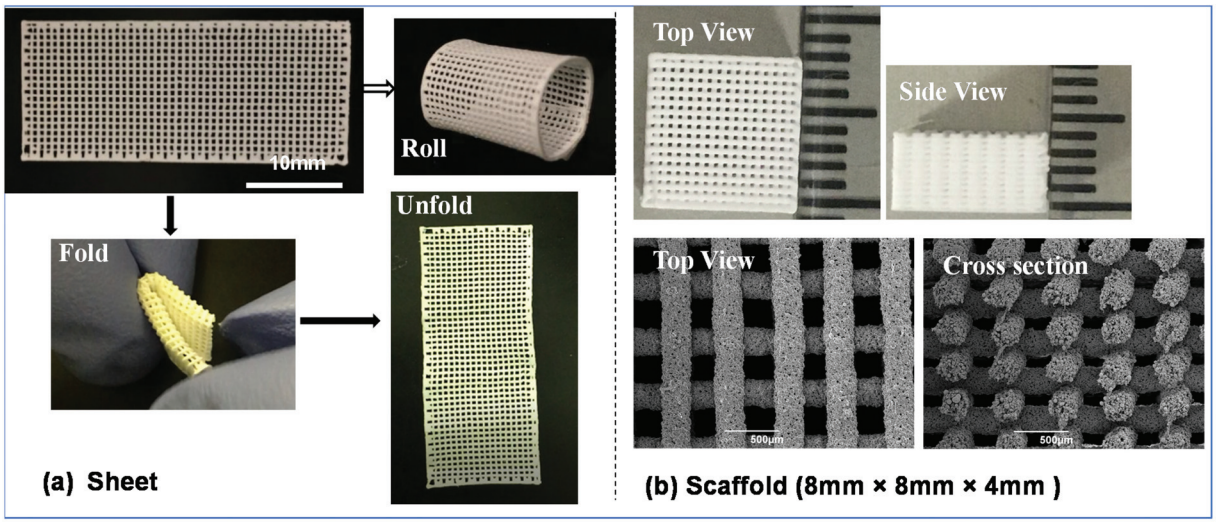

Fig. 1 3D printed sheet and scaffold consisting of PEG400/PCL/HA composite struts (mass ratio PEG : PCL : HA = 7 : 10 : 90). (a) Rolling, folding and unfolding of a printed sheet (4 layers). (b) Gross views and SEM images of a printed thick scaffold.

respectively. For struts with PEG(400), the ductility of struts increased at lower PEG : PCL ratios, indicating better plasticizing effect of PEG400. The ductility of struts with PEG400 was better before immersion in contrast to those with higher molecular weight PEGs. When the mass ratio of PEG400 : PCL reached 7 : 10, the breaking strain was 260.9% and reduced to 121.2% after immersion but still ductile.

The tensile moduli and strengths of the struts before and after immersion in water are shown in Fig. 3. For PEG(20k) and PEG(3350), PEG showed only marginal effect on the modulus and strength when the PEG : PCL ratio was 5 : 10 and lower before immersion. The elastic modulus and strength decreased when the ratio was 7 : 10 and higher. For struts with PEG(400) the moduli were lower than those with PEG(20k) and PEG(3350) at all three ratios (3 : 10, 5 : 10 and 7 : 10). In contrast to the two high molecular weight PEGs, the moduli of struts with PEG(400) increased after immersion. Immersion in water showed relatively less effect to strength compared to modulus. It is worth noting that immersion showed no significant effect for the PCL/HA struts without PEG. The mass of struts dropped rapidly after immersion in water for 30 minutes, then kept almost constantly up to 28 days (Fig. S6†). Mass reduction showed that the mass losses were almost equal to the amounts of PEG that were added to the struts, suggesting most of the PEG leached out after immersion in water for 30 minutes (Fig. S6†).

3.2. Effect of HA concentration on the mechanical properties of struts and scaffolds

PEG(400) was demonstrated to be a better plasticizer to endow ductility to the composite struts as less PEG(400) was required to increase breaking strain (Fig. 2). PEG(400) was therefore selected as the plasticizer with a fixed mass ratio of PEG (400) : PCL at 7 : 10. The mechanical properties of struts with different HA contents (72 wt%, 84 wt% and 90 wt%, 94 wt%) were then tested. These HA concentrations represent the percentages of HA in the total mass of HA and PCL as PEG leaches out during immersion.

Fig. 4 shows the tensile mechanical properties of struts with various HA contents. Before immersion in water, the elastic modulus, ultimate tensile strength and breaking strain decreased with the increasing HA concentration. The trend was largely the same for immersed struts that had PEG leached out. It is worth noting that the struts with the highest HA concentration (94 wt%) were ductile before immersion, albeit with a lower breaking strain of 92.4%. However, the ductility disappeared for these struts after 24 hours of immersion in water.

After measuring the individual struts, the tensile mechanical properties of 3D printed scaffolds made of PEG(400)/PCL/HA were then tested. Fig. 5 shows the tensile properties of 3D printed scaffolds consisting of the ductile struts. As the scaffolds were porous, the mechanical properties of the scaffolds were much lower than the individual struts. The breaking strains of the scaffolds were also significantly lower than the individual struts, though still larger than 100%, meaning ductility of the 3D printed scaffolds.

Fig. 6 shows the results of the compression testing of the scaffolds with various HA concentrations. The compressive properties of the scaffolds demonstrated similar trends to the tensile properties of struts. As the HA concentration increased, both compressive yield strength and modulus decreased. After

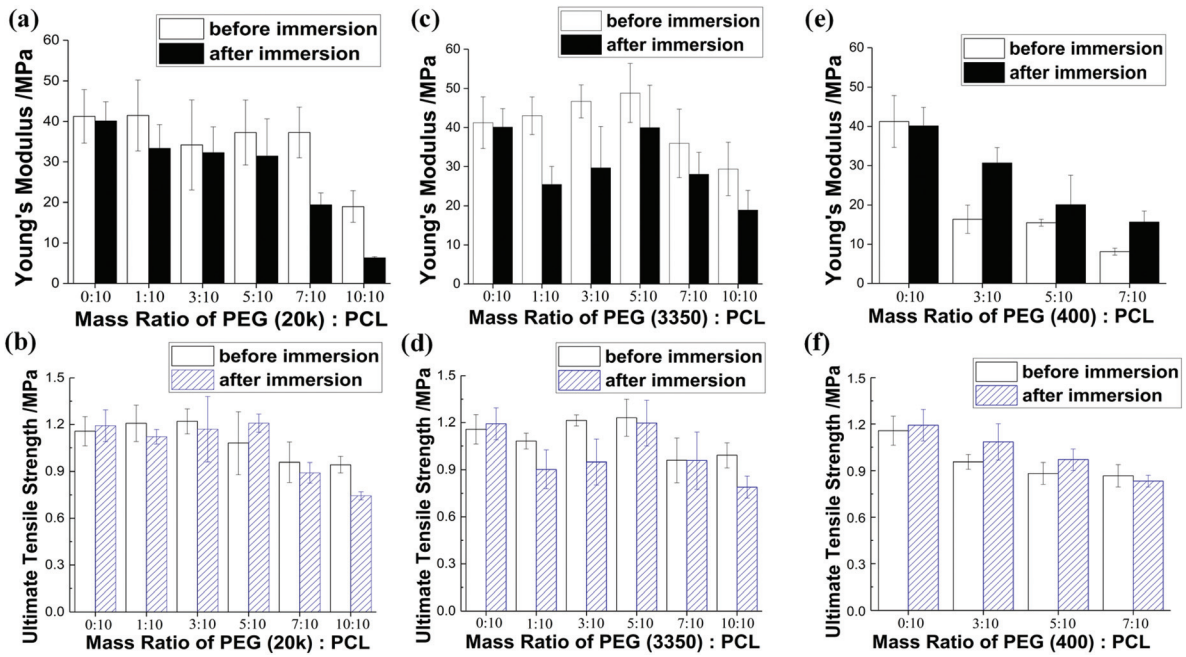

Fig. 3 Modulus and strength measured using single strut tensile testing. (a and b) PEG(20k)/PCL/HA, (c and d) PEG(3350)/PCL/HA, (e and f) PEG (400)/PCL/HA. The mass ratio of PCL to HA was fixed at 1 : 9. Data represent mean ± SD, n = 5.

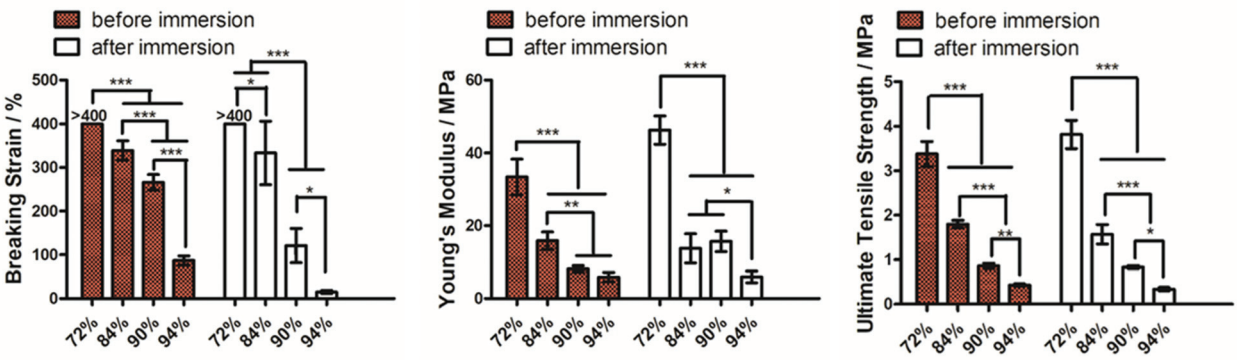

Fig. 4 Breaking strain, Young's modulus and Ultimate tensile strength of the PCL/PEG400/HA struts (mass ratio PEG(400) : PCL = 7 : 10) with different HA concentrations. Data represent mean ± SD, n = 5. * indicates $p < 0.05$, ** indicates $p < 0.01$ and *** indicates $p < 0.001$.

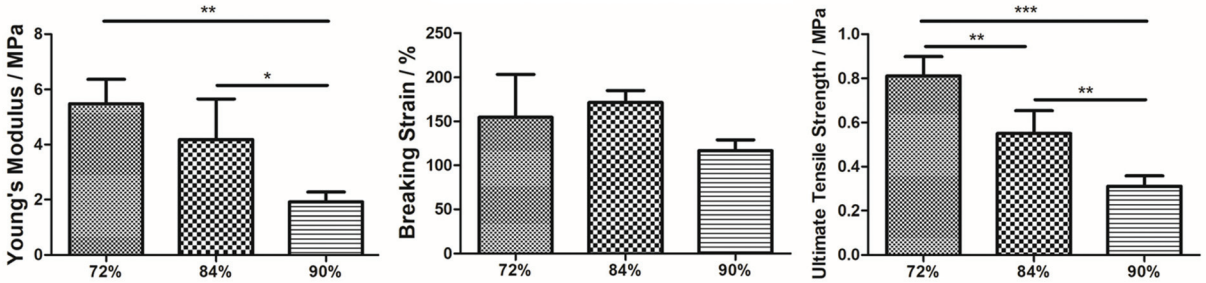

Fig. 5 Tensile properties of 3D printed scaffolds (6 layers) consisting of ductile struts. Data represent mean ± SD, n = 4. * indicates $p < 0.05$, ** indicates $p < 0.01$ and *** indicates $p < 0.001$.

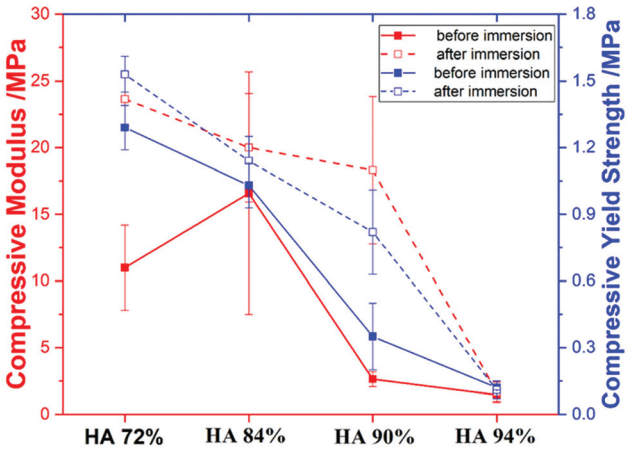

Fig. 6 Compression modulus and yield strength of PCL/PEG(400)/HA scaffolds with different HA concentrations. Data represent mean ± SD, n = 3. Lines are used only for guiding the eyes.

immersion, the compressive yield strength and modulus increased, especially for the 90% HA scaffolds which increased from 0.35 MPa and 2.64 MPa to 0.82 MPa and 18.31 MPa for yield strength and modulus, respectively. The increase in modulus of the scaffolds after immersion was consistent with what was observed for the struts with PEG(400).

3.3 Morphology of PCL/PEG/HA struts with different HA concentrations

Fig. 7 shows the SEM images of PCL/PEG(400)/HA scaffolds with various HA concentrations (72 wt%, 84 wt%, 90 wt%, and 94 wt%). The surface of the 72% HA scaffold was relatively smoother than the others with some HA micro particles visible on the strut surface. There seemed to be more presence of HA particles in the 72% HA scaffolds after immersion in water. As the HA concentration increased, there was significantly more exposure of the HA particles. The levels of HA exposure for the 84%, 90% and 94% HA scaffolds were similar. There were visible pores between the HA particles in the struts when the HA concentration was higher than 72%. Besides the pores between the HA particles, microscopic pores were visible within the polymer matrix for the 84% HA and 90% HA scaffolds (Fig. 7 insets). These pores might be due to the phase separation between PCL and PEG.[38] However, the 94% HA scaffold showed no sign of pores within the polymer matrix, possibly due to the very small amount of PCL and PEG in the composite.

3.4 *In vitro* osteogenic differentiation and *In vivo* bone regeneration in rat calvarial defects

We first characterized *in vitro* osteogenic differentiation of human mesenchymal stem cells within three different 3D

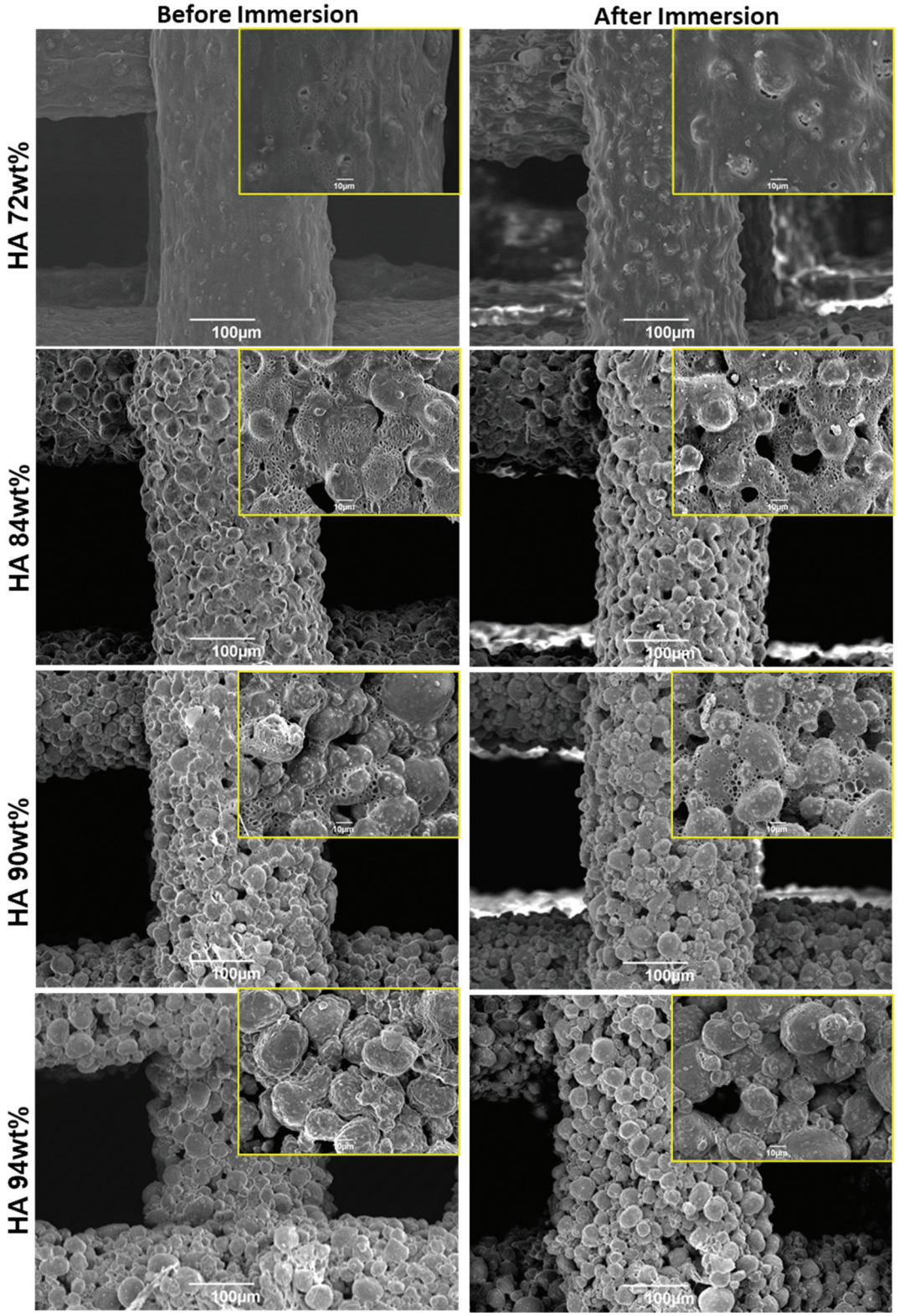

Fig. 7 SEM images of PCL/PEG(400)/HA scaffolds with varied HA concentrations. Insets show the high-magnification images of strut surfaces. The scale bars in insets are 10 μm.

printed scaffolds (Pure PCL, 72 wt% and 90 wt%). The actual hydroxyapatite contents in these scaffolds quantified by thermogravimetric analysis were similar to the theoretical values (Fig. S7†). Osteocalcin was selected as an osteogenic differentiation marker. Cell proliferation and secretion of osteocalcin are shown in Fig. 8. hMSCs proliferated with similar rates between the three different types of scaffolds. The amount of osteocalcin (normalized to DNA content) was significantly higher for the 90% HA scaffolds. Soaking scaffolds in simulated body fluid appeared to cause more apatite formation on the 90% HA scaffolds (Fig. S8†). The enhanced osteogenic differentiation for the 90% HA scaffolds might be attributed to the increased strut surface mineralization. Cell attachment and morphology within the scaffolds during *in vitro* cell cultivation were also monitored using SEM (Fig. S9†). Cell attachment and spreading were visible in all scaffolds.

We then characterized bone regeneration using a rat calvarial model. Scaffolds with two HA concentrations (72 wt% and 90 wt%) were implanted in rat calvarial defects. PEG within the scaffolds was not removed before implantation. The two HA concentrations were selected based on the distinct difference in the presence of HA on the strut surfaces. In addition, the 94% HA scaffolds were mechanically weak during manual handling.

Fig. 9 shows the gross morphology, micro-CT images and H&E staining of the retrieved scaffolds after 12 weeks *in vivo*. The scaffolds largely maintained their shape after implantation for 12 weeks. Given the slow degradation rate of both PCL and HA, it was not expected to see significant degradation during the *in vivo* testing period. According to the gross morphology, more scaffolds of the 72% HA group showed translucent fibrous tissue within them. The regenerated tissues within the 90% HA scaffolds appeared to be denser than those in the 72% HA scaffolds. The micro-CT images showed that the pores of the scaffolds were not completely mineralized and varied levels of mineralization were apparent. Comparing the gross morphology to the micro-CT images, it was clear that not all the optically opaque tissues have been mineralized. Comparing the H&E staining to micro-CT images, areas within the scaffolds that were stained brightly pink by Eosin, similar to the host bone at both ends of the scaffolds, were new bone. Locations that were stained less intensively pink appeared to be fibrous tissue. Whilst most new tissue appeared to be within the pores some scaffolds (sample 4, 10) showed new bone on the scaffold surface as demonstrated by the microCT images and the H&E staining.

Quantification of the Eosin-stained area showed that there was significantly more matrix in the 90% HA scaffolds (Fig. 10). However, when mineral volume within the scaffold pores was quantified using the microCT images, it was not statistically different between the two types of scaffolds (Fig. 10). It was not possible to differentiate new bone from the scaffolds during the quantification of the microCT images, hence scaffolds and new bone were combined as mineral volume.

To investigate the tissue formed with the pores of the scaffolds in more detail, higher magnification images were taken from the H&E stained samples (Fig. 11 and Fig. S10†). Fibrous tissue surrounded the struts with aligned collagen fibres conforming with the contour of the struts. It was consistently observed that more cells infiltrated into the struts of the 90% scaffolds compared to those of the 72% scaffolds (Fig. S10†). This was likely caused by the fact that the struts with 90% HA were more porous than those in the 72% HA scaffolds (Fig. 7). Multinucleated cells have been commonly found surrounding the struts (Fig. 11, Fig. S10†). Blood vessels are commonly seen within the fibrous tissue with erythrocytes stained brightly pink within them. The amount of blood

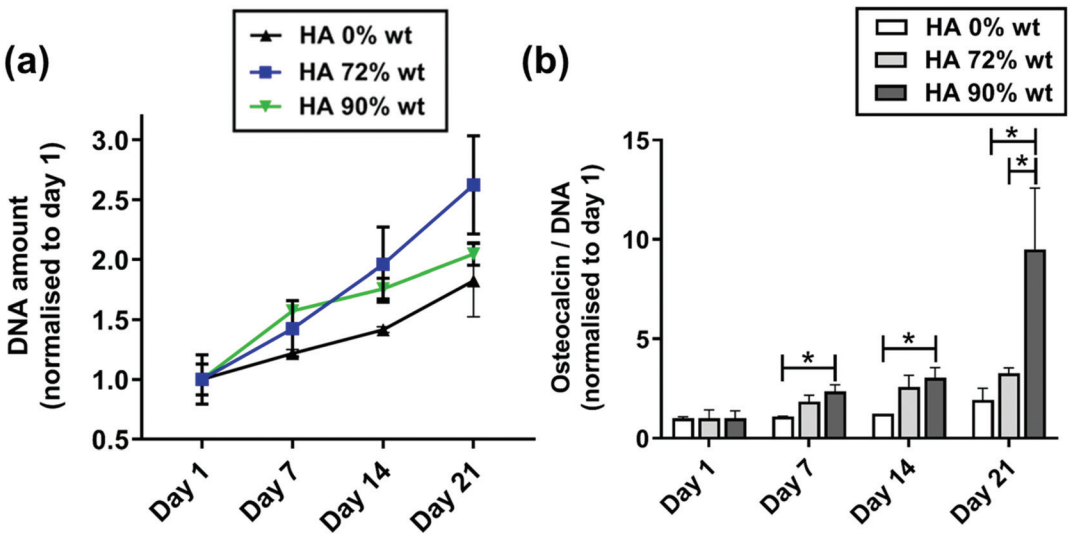

Fig. 8 DNA content and osteocalcin secretion of *in vitro* cultured immortalised hMSCs within three different scaffolds. Data represent mean ± SD, $n = 3$. * indicates $p < 0.05$.

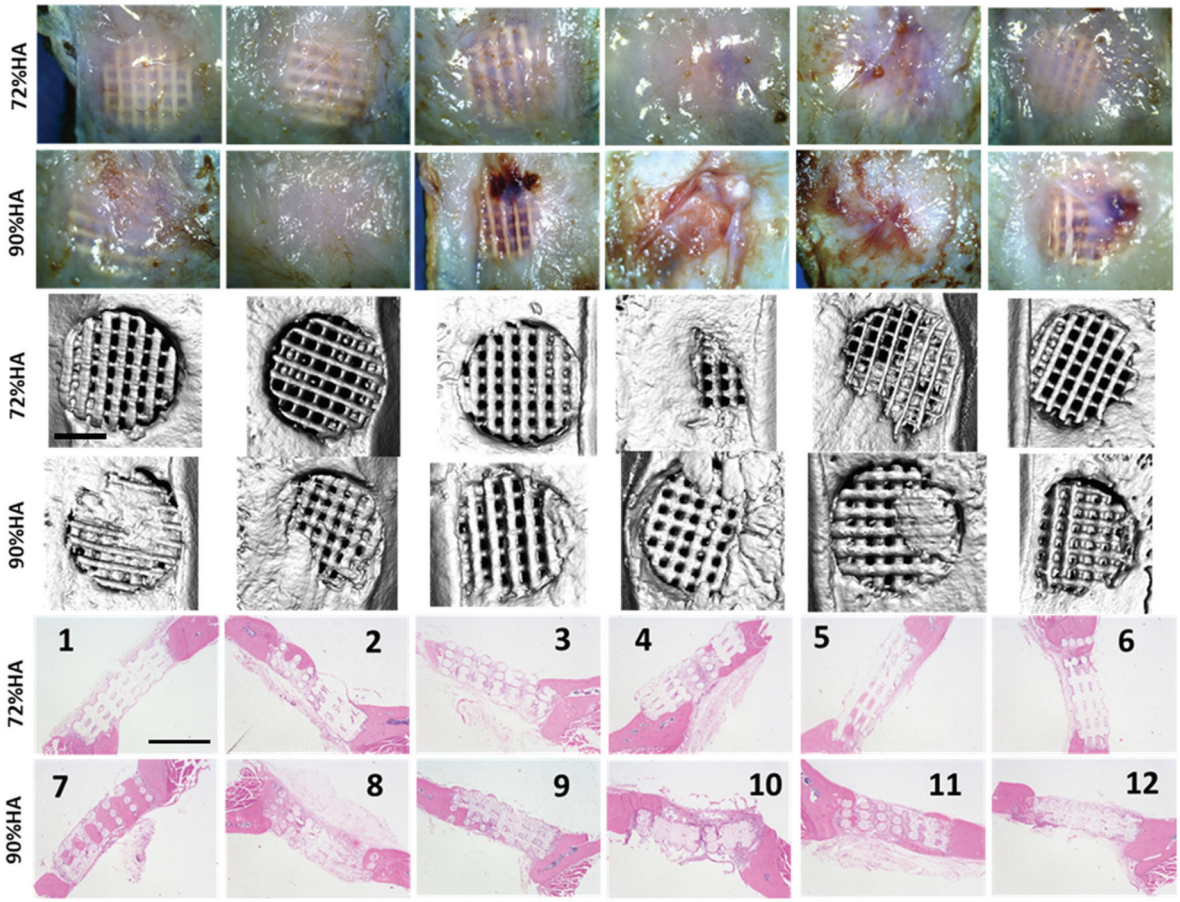

Fig. 9 Image of scaffolds after 12-week implantation in rat calvarial defects. Row 1&2 – Gross morphology of retrieved scaffolds. Row 3&4 – MicroCT images of the scaffolds. Row 5&6 – H&E staining (pink staining) of transverse cross-sectional slices of the scaffolds. Six samples were tested for each scaffold composition. Scale bars are 2 mm.

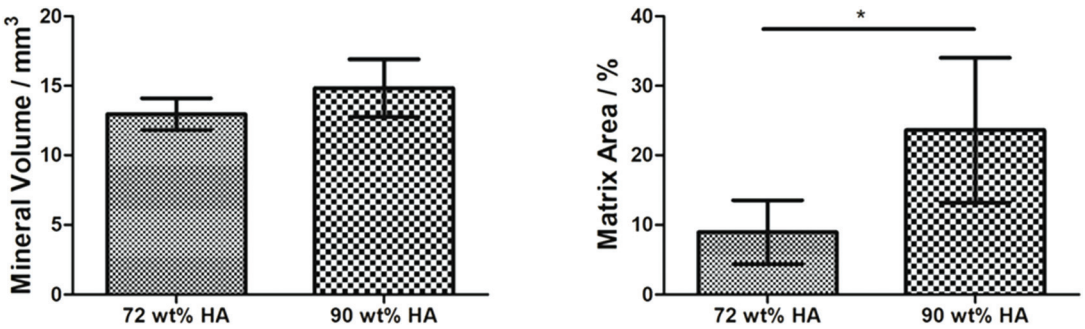

Fig. 10 Mineral volume (including both new bone and scaffold) and quantified matrix area (Eosin stained) within scaffolds. * denotes $p < 0.05$, Data represent mean ± SD, $n = 6$.

vessels was comparable between the two types of scaffolds when vessel areas were quantified in the H&E staining images (Fig. 11c). 70% HA scaffolds which mostly had fibrous tissues within the pores also contained a good amount of blood vessels (Fig. 11b).

As some tissue within the 90% HA scaffolds that were optically dense but not mineralized resembled cartilage, in conjunction with the aim to identify the route of bone formation, expression of collagen II (chondrogenic markers) was analysed using immunohistochemistry (Fig. 12). In general, the level of collagen II presence within the scaffold was low. In addition, collagen II was not evenly distributed in the tissue within the pores (Fig. 12, Fig. S11†). Some areas showed relatively more intensive staining of collagen II, which might be an indication

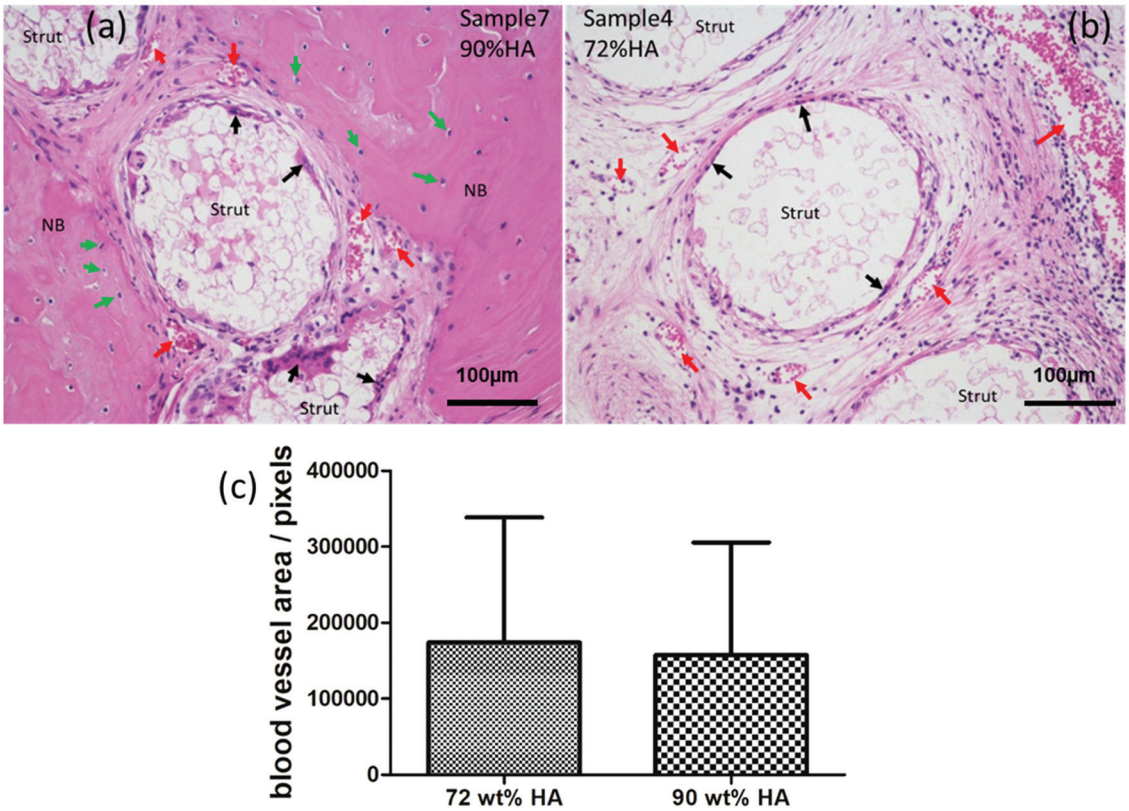

Fig. 11 High magnification images of H&E staining of (a) 90% HA and (b) 72% HA scaffold. The presence of blood vessels, multinucleated cells and osteocytes within regenerated bone are visible. Red arrow – blood vessel; black arrow – multinucleated cells; Green arrow – osteocyte; NB – new bone. (c) Quantified blood vessel area from H&E images. Blood vessel areas were manually selected in individual images and quantified by using ImageJ. Date represent mean ± SD, n = 18.

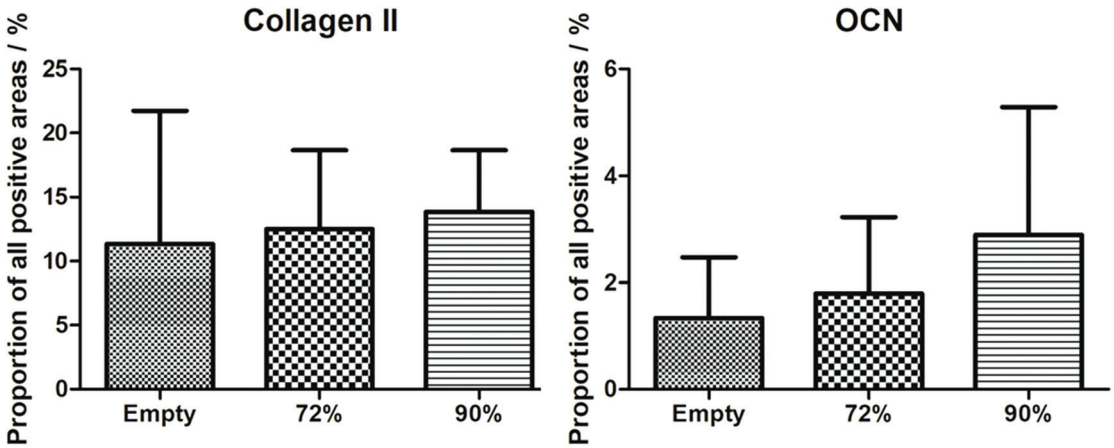

Fig. 12 Quantified immunostaining of collagen II and OCN of the 72% HA and 90% HA scaffolds. The images used for quantification are included in Fig. S12 and 13.†

of difference in cellular differentiation status. OCN was also stained as an osteogenic differentiation marker. Although quantification of OCN appeared to be higher in the 90% HA scaffolds, but there was no statistical difference between the compared groups (Fig. 12).

For scaffolds that had new bone formation, immunostaining of collagen II and H&E staining revealed that new bone regenerated in the pores was formed *via* intramembranous ossification (Fig. 13). Fig. 13a and 13b are H&E and collagen II staining of the same 72% HA scaffold. The central

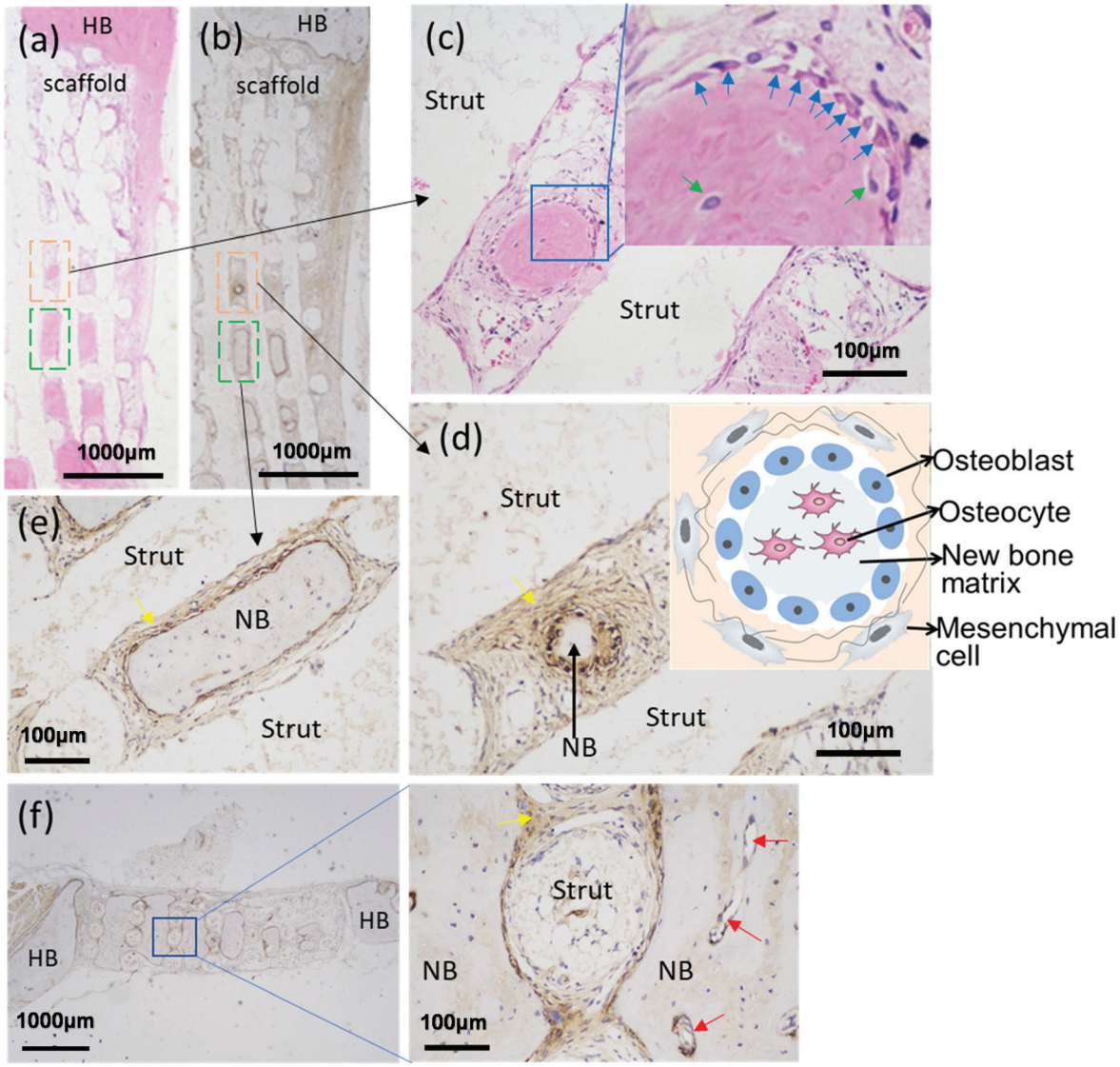

Fig. 13 H&E staining and immunostaining of collagen II (brown). (a) H&E staining and (b) Immunostaining of collagen II of the same 72% HA scaffold showing tissue formed within the pores. (c–e) are high-magnification images of the areas within the dashed boxes. Inset in (d) is a schematic of intramembranous ossification. (f) Immunostaining of collagen II of a 90% HA scaffold. Blue arrow–cells morphologically resemble osteoblasts; Green arrow – osteocyte; Yellow arrow – fibrous tissue; Red arrow – blood vessel; NB – new bone; HB – host bone.

region of the eosin stained new bone showed absence of collagen II (Fig. 13d and e). The presence of collagen II was most intensive in areas that immediately surrounded the new bone (Fig. 13d–f). The morphology of the new bone tissue represents the process of bone formation *via* intramembranous ossification in which mesenchymal cells condense and differentiate to osteoblasts that secret osteoid (Fig. 13d inset).[27]

4 Discussion

This study aimed to test: (1) the effectiveness of PEG on endowing ductility to PCL/HA composites with high HA concentrations; (2) how the level of HA exposure on strut surface affects bone regeneration; and (3) the route of bone regeneration within the pores (pores between struts) of the 3D printed scaffolds *in vivo*. PEG was chosen because of its biocompatibility and demonstrated plasticizing effect on polymers.[39,40] In this study, PCL/PEG/HA composites with high HA contents were endowed with ductility by adding PEG alone, which means there is no need to wash the scaffolds after printing to remove hazardous additives. In addition, our previous data showed that residual DCM in 3D printed scaffolds can evaporate to safe levels in air.[41]

PEG with lower molecular weight (400 Da) was shown to be a better plasticizer as the ductility of struts (increased breaking strain) was achieved with a lower concentration. One study reported the effect of the molecular weight of PEG on the

toughness of PCL/PEG/Starch blends, which showed an optimal molecular weight of 3400 Da (when compared against 400, 8000 and 100 000 Da) for maximum toughness and breaking strain.[42] However, this three-component blend is different from the ones in our study, and the toughness depended on the interaction between the three components and the interaction between PEG(400) and PCL was shielded by starch.

Instead of a gradual increase of ductility with increasing PEG content as reported before,[40] our results showed a dramatic increase in ductility after reaching a threshold of PEG : PCL ratio which is molecular weight dependent (7 : 10 for PEG(400), 10 : 10 for PEG(3350) and PEG(20k)). For struts with PEG(3350) and PEG(20k) which are solid at room temperature, ductility was obtained only after the struts were immersed in water. The increase in ductility after immersion may be attributed to the removal of brittle PEG-rich domains which might be formed as a result of the phase separation between PEG and PCL.[38] It was found that the ductility was largely maintained or improved even after most PEG leached out after immersion (Fig. 2, Fig. S5†). Interestingly when a relatively small amount of PEG was added (PEG : PCL < 5 : 10), the increase in failure strain was marginal. This may be due to that the free volume created by the plasticizer (PEG) was still present after the leaching out of PEG.[43] Indeed, ductility disappeared after annealing the struts which removed the free volume created by the addition of PEG (Fig. S14†).

In general, the elastic modulus and strength of the struts and scaffolds decreased with increasing HA content (Fig. 4–6). This is likely due to the decreasing amount of PCL matrix which binds the particles together and consequently the reduced ability in transferring load from the polymer matrix to the HA particles.[44] It was clear from the SEM images that higher concentration of HA particles in the struts resulted in more apparent exposure of them on the strut surface, particularly when the concentration was higher than 70 wt% (Fig. 7). The trade-off between mechanical properties and the amount of exposed HA particles on the strut surface led us to study the effect of HA concentration on the formation of bone *in vivo* to identify if high-concentration HA is beneficial for bone formation. The *in vivo* data demonstrated that more HA exposure on strut surface (90% HA scaffolds) enhanced matrix formation within the pores, but not mineral volume compared to the 72% HA scaffolds. Previous studies have reported beneficial effect of higher ceramic concentration on osteogenesis. However, the reported ceramic concentrations were lower than the ones studied here.[45] The long-term effect of high HA concentration on bone regeneration requires further investigation. It is worth noting that the strut topography was different between the two types of scaffolds. There is ample evidence that topography affects the differentiation of mesenchymal stem cells *in vitro*.[46] However, effect of topography on bone regeneration *in vivo* is less clear[47] though improved osseointegration associated with implant surface roughness has been reported before.[48] Although the compressive mechanical properties of the scaffolds are inferior to cortical bones, they are within the lower end of the mechanical property range of cancellous bone.[49,50] It is envisaged that the 3D printed ductile scaffolds could be used in non-load bearing applications for bone regeneration. For them to be used in load-bearing applications, innovative ways of mechanically reinforcing these high-inorganic-concentration struts will need to be explored in the future.

Histological analyses (H&E staining, Immunohistochemistry of collagen II) were carried out to study the tissues formed within the pores in more detail and to exam the route of bone formation within 3D printed scaffolds, which is under-investigated. Moreover, a recent study reported endochondral ossification induced by aligned pores within collagen sponges which have some level of resemblance to the regular pore arrangement in 3D printed scaffolds.[51] Therefore, it was intriguing to investigate how bone is formed within the 3D printed scaffolds. According to the gross morphologies, the tissues formed in the 72% HA scaffolds appeared to be more translucent and less dense compared to those within the 90% HA scaffolds. The fibrous tissue found in the scaffolds resembles what has been observed in non-union bone fractures in humans.[52] Some visually opaque white tissues that were not mineralized according to microCT images resembled cartilage. Therefore, immunostaining of collagen II was carried out to study if those tissues were cartilaginous. Neither large areas that showed intensively stained collagen II nor cells morphologically resemble chondrocytes were found. Instead, as demonstrated by H&E staining and immunohistochemistry of collagen II, bone within the pores was regenerated *via* intramembranous ossification. During intramembranous ossification a condensation of mesenchymal cells develops, within which osteoblasts differentiate and deposit mainly collagen type I with some type II and III,[27,53] which explains the presence of some collagen II surrounding the new bone. It was noticed that collagen II was not evenly distributed in the fibrous tissues with some areas having relatively higher levels (Fig. 13, Fig. S11†), which indicated that the mesenchymal cell population within the fibrous tissue may consists of sub-populations that were functionally different. Partial dissolution of hydroxyapatite followed by the formation of carbonated hydroxyapatite has been reported to trigger a mineralization of the ECM leading to bone formation,[54] which has been considered to contribute to the bonding between hydroxyapatite and host bone. However, bone formation within the pores appeared to start in the central region rather than initiating from the strut surface (Fig. 13). Some pores with bone formation have shown proximity between the new bone and the strut surface whilst others have shown a relatively thicker fibrous layer between the new bone and the strut surface (Fig. 13). New bone within these pores might continue growing until it meets the strut surface.

Comparing scaffolds with varied levels of bone formation, the amount of blood vessels did not appear to be significantly different among them (Fig. 11). This suggests that the level of vascularization, while important for progenitor cell recruitment and transportation of oxygen and nutrients, is not a responsible factor for the varying levels of bone regeneration

within the different scaffolds. This is similar to what has been reported in literature in which no significant difference was evident in the vessel count between atrophic/hypertrophic non-unions and normal unions.[55] Multinucleated cells were commonly observed surrounding the struts. It is likely that these cells are multinucleated giant cells given their close association with the struts, which is a hallmark of foreign body reaction (FBR). It was not surprising to find the presence of these cells as FBR is common in biomaterial implants and PCL and HA degrade slowly.[56] On the other hand, osteoclasts are multinucleated cells derived from the fusion of mononuclear precursors belonging to the monocyte/macrophage lineage.[57] Bone remodeling relies on the actions of both osteoclasts and osteoblasts. The presence of these multinucleated cells may accelerate the degradation of HA *in vivo.*[58] Moreover, immune response is an intimate part of bone fracture healing.[59] Inflammatory response elicited by bone injury is beneficial to healing when it is acute and regulated. However, if this process is dysregulated and chronic, inflammation can be detrimental to healing.[60] Mesenchymal stem/progenitor cells have been found in non-union tissues despite little bone regeneration being present in the fracture sites.[61] Senescence of stem/progenitor cells presents one of the main mechanisms of the loss of the regenerative potential leading to healing impairment. Mesenchymal stromal cells isolated from atrophic non-union tissues have shown senescence and a reduced capacity to differentiate into mature and functional osteoblasts.[62] The varied level of bone formation within the scaffolds may hence be linked to the level of inflammation sensed by the stromal cells in the tissue within the pores. Where new bone was formed within the scaffold pores, a layer of fibrous tissue between struts and new bone was often observed, which may be an indication of the inhibitory effect of prolonged inflammation on bone formation. However, the functionality of these stromal cells, particularly their osteogenic potential and their interactions with immune cells, need more detailed analysis in the future.

5 Conclusion

3D printed scaffolds that are osteoconductive and have sufficient mechanical properties for bone tissue engineering are urgently needed. The route of bone formation within these scaffolds also requires detailed analysis. PEG has been demonstrated to be an effective plasticizer to make high-HA-concentration (up to 90 wt% HA) scaffolds ductile. The failure strain of individual struts increased significantly from 6.2% to 260.9% by adding PEG400. These 3D printed PCL/PEG/HA scaffolds did not require further post-printing washing to remove hazardous components before implantation. More HA exposure caused by high HA concentration was demonstrated to enhance matrix formation though at a cost of lower modulus and strength of the scaffolds. However, the mechanical properties were still within the range of cancellous bone and sufficient for non-load bearing applications. Moreover, we have demonstrated that new bone within the pores of 3D printed scaffolds was formed *via* intramembranous ossification and started from the central region of pores. The amount of blood vessels formed within the pores did not seem to be significantly different between scaffolds with varied bone formation. The data has also suggested a role of immune response associated with the presence of synthetic biomaterials on bone regeneration, which warrants further investigation.

Conflicts of interest

There are no conflicts to declare.

Acknowledgements

The authors thank the Development and Promotion of Science and Talent Project (DPST) for sponsoring Aruna Prasopthum's studentship and Nanoscale and Microscale Research Centre (NMRC) at University of Nottingham for electron microscope facilities. The authors also thank the Chinese Scholarship Council for supporting Dr Chuanliang Cao's academic visit to Dr Jing Yang' group.

References

1 M. A. Woodruff, *et al.*, Bone tissue engineering: from bench to bedside, *Mater. Today*, 2012, **15**(10), 430–435.
2 H. S. Ma, *et al.*, 3D-printed bioceramic scaffolds: From bone tissue engineering to tumor therapy, *Acta Biomater.*, 2018, **79**, 37–59.
3 S. Bose, *et al.*, Bone tissue engineering using 3D printing, *Mater. Today*, 2013, **16**(12), 496–504.
4 D. Tang, *et al.*, Biofabrication of bone tissue: approaches, challenges and translation for bone regeneration, *Biomaterials*, 2016, **83**, 363–382.
5 H. F. Shao, *et al.*, Bone regeneration in 3D printing bioactive ceramic scaffolds with improved tissue/material interface pore architecture in thin-wall bone defect, *Biofabrication*, 2017, **9**(2), 025003.
6 J. Malda, *et al.*, The effect of PEGT/PBT scaffold architecture on the composition of tissue engineered cartilage, *Biomaterials*, 2005, **26**(1), 63–72.
7 S. Ghouse, *et al.*, The design and in vivo testing of a locally stiffness-matched porous scaffold, *Appl. Mater. Today*, 2019, **15**, 377–388.
8 J. T. Zhang, *et al.*, Calcium phosphate cements for bone substitution: Chemistry, handling and mechanical properties, *Acta Biomater.*, 2014, **10**(3), 1035–1049.
9 Y. Luo, *et al.*, Three-Dimensional Printing of Hollow-Struts-Packed Bioceramic Scaffolds for Bone Regeneration, *ACS Appl. Mater. Interfaces*, 2015, **7**(43), 24377–24383.
10 A. Nommeots-Nomm, *et al.*, Direct ink writing of highly bioactive glasses, *J. Eur. Ceram. Soc.*, 2018, **38**(3), 837–844.

11 A. A. Sawyer, *et al.*, The stimulation of healing within a rat calvarial defect by mPCL-TCP/collagen scaffolds loaded with rhBMP-2, *Biomaterials*, 2009, **30**(13), 2479–2488.
12 S. L. McNamara, *et al.*, Silk as a biocohesive sacrificial binder in the fabrication of hydroxyapatite load bearing scaffolds, *Biomaterials*, 2014, **35**(25), 6941–6953.
13 S. I. Roohani-Esfahani, *et al.*, Design and Fabrication of 3D printed Scaffolds with a Mechanical Strength Comparable to Cortical Bone to Repair Large Bone Defects, *Sci. Rep.*, 2016, **6**, 19468.
14 S. Yang, *et al.*, The design of scaffolds for use in tissue engineering. Part I. Traditional factors, *Tissue Eng.*, 2001, **7**(6), 679–689.
15 I. Tcacencu, *et al.*, Osseointegration of porous apatite-wollastonite and poly(lactic acid) composite structures created using 3D printing techniques, *Mater. Sci. Eng., C*, 2018, **90**, 1–7.
16 P. S. P. Poh, *et al.*, In vitro and in vivo bone formation potential of surface calcium phosphate-coated polycaprolactone and polycaprolactone/bioactive glass composite scaffolds, *Acta Biomater.*, 2016, **30**, 319–333.
17 K. K. Moncal, *et al.*, 3D printing of poly(epsilon-caprolactone)/poly(D,L-lactide-co-glycolide)/hydroxyapatite composite constructs for bone tissue engineering, *J. Mater. Res.*, 2018, **33**(14), 1972–1986.
18 F. H. Lin, *et al.*, The merit of sintered PDLLA/TCP composites in management of bone fracture internal fixation, *Artif. Organs*, 1999, **23**(2), 186–194.
19 A. Bruyas, *et al.*, Systematic characterization of 3D-printed PCL/β-TCP scaffolds for biomedical devices and bone tissue engineering: influence of composition and porosity, *J. Mater. Res.*, 2018, **33**(14), 1948–1959.
20 B. Chuenjitkuntaworn, *et al.*, Polycaprolactone/Hydroxyapatite composite scaffolds: Preparation, characterization, and in vitro and in vivo biological responses of human primary bone cells, *J. Biomed. Mater. Res., Part A*, 2010, **94A**(1), 241–251.
21 O. Guillaume, *et al.*, Surface-enrichment with hydroxyapatite nanoparticles in stereolithography-fabricated composite polymer scaffolds promotes bone repair, *Acta Biomater.*, 2017, **54**, 386–398.
22 M. Bohner, *et al.*, β-tricalcium phosphate for bone substitution: Synthesis and properties, *Acta Biomater.*, 2020, **113**, 23–41.
23 J. R. Jones, Review of bioactive glass: From Hench to hybrids, *Acta Biomater.*, 2013, **9**(1), 4457–4486.
24 A. E. Jakus, *et al.*, Hyperelastic "bone": A highly versatile, growth factor-free, osteoregenerative, scalable, and surgically friendly biomaterial, *Sci. Transl. Med.*, 2016, **8**(358), 358ra127.
25 *Limiting the Use of Certain Phthalates as Excipients in CDER-Regulated Products*. 2012; Available from: https://www.fda.gov/regulatory-information/search-fda-guidance-documents/limiting-use-certain-phthalates-excipients-cder-regulated-products#_Toc462221103.
26 S. Stewart, *et al.*, *Translational Regenerative Medicine*, ed. A. Atala and J. G. Allickson, 2015, Academic Press, Boston. pp. 313–333.
27 T. A. Franz-Odendaal, *et al.*, Buried alive: how osteoblasts become osteocytes, *Dev. Dyn.*, 2006, **235**(1), 176–190.
28 E. J. Mackie, *et al.*, Endochondral ossification: how cartilage is converted into bone in the developing skeleton, *Int. J. Biochem. Cell. Biol.*, 2008, **40**(1), 46–62.
29 N. Harada, *et al.*, Bone regeneration in a massive rat femur defect through endochondral ossification achieved with chondrogenically differentiated MSCs in a degradable scaffold, *Biomaterials*, 2014, **35**(27), 7800–7810.
30 E. M. Thompson, *et al.*, An Endochondral Ossification-Based Approach to Bone Repair: Chondrogenically Primed Mesenchymal Stem Cell-Laden Scaffolds Support Greater Repair of Critical-Sized Cranial Defects Than Osteogenically Stimulated Constructs In Vivo, *Tissue Eng., Part A*, 2016, **22**(5–6), 556–567.
31 E. J. Sheehy, *et al.*, Engineering cartilage or endochondral bone: a comparison of different naturally derived hydrogels, *Acta Biomater.*, 2015, **13**, 245–253.
32 G. Liu, *et al.*, Cytotoxicity study of polyethylene glycol derivatives, *RSC Adv.*, 2017, **7**(30), 18252–18259.
33 F. M. Veronese, *et al.*, PEGylation, successful approach to drug delivery, *Drug Discovery Today*, 2005, **10**(21), 1451–1458.
34 T. Okamoto, *et al.*, Clonal heterogeneity in differentiation potential of immortalized human mesenchymal stem cells, *Biochem. Biophys. Res. Commun.*, 2002, **295**(2), 354–361.
35 C. Zong, *et al.*, Reconstruction of rat calvarial defects with human mesenchymal stem cells and osteoblast-like cells in poly-lactic-co-glycolic acid scaffolds, *Eur. Cells Mater.*, 2010, **20**, 109–120.
36 J. A. McGovern, *et al.*, Animal models for bone tissue engineering and modelling disease, *Dis. Model Mech.*, 2018, **11**(4), dmm033084.
37 F. Varghese, *et al.*, IHC Profiler: an open source plugin for the quantitative evaluation and automated scoring of immunohistochemistry images of human tissue samples, *PLoS One*, 2014, **9**(5), e96801.
38 W.-T. Chuang, *et al.*, Kinetics of Phase Separation in Poly(ε-caprolactone)/Poly(ethylene glycol) Blends, *J. Polym. Res.*, 2005, **12**(3), 197–204.
39 D. C. Li, *et al.*, Preparation of plasticized poly (lactic acid) and its influence on the properties of composite materials, *PLoS One*, 2018, **13**(3), 0193520.
40 W. Pivsa-Art, *et al.*, The effect of poly(ethylene glycol) as plasticizer in blends of poly(lactic acid) and poly(butylene succinate), *J. Appl. Polym. Sci.*, 2016, **133**(8), 43044.
41 A. Prasopthum, *et al.*, Three-Dimensional Printed Scaffolds with Controlled Micro-/Nanoporous Surface Topography Direct Chondrogenic and Osteogenic Differentiation of Mesenchymal Stem Cells, *ACS Appl. Mater. Interfaces*, 2019, **11**(21), 18896–18906.
42 C. H. Kim, *et al.*, Effect of PEG molecular weight on the tensile toughness of starch/PCL/PEG blends, *J. Appl. Polym. Sci.*, 2000, **77**(9), 2049–2056.
43 E. Langer, *et al.*, *Plasticizers Derived from Post-Consumer PET*, ed. E. Langer, *et al.*, William Andrew Publishing. 2020, p. 1–11.

44 S.-Y. Fu, *et al.*, Effects of particle size, particle/matrix interface adhesion and particle loading on mechanical properties of particulate–polymer composites, *Compos., Part B*, 2008, **39**(6), 933–961.
45 B. Y. Huang, *et al.*, Polymer-Ceramic Composite Scaffolds: The Effect of Hydroxyapatite and beta-tri-Calcium Phosphate, *Materials*, 2018, **11**(1), 129.
46 M. J. Dalby, *et al.*, Harnessing nanotopography and integrin-matrix interactions to influence stem cell fate, *Nat. Mater.*, 2014, **13**(6), 558–569.
47 A. Wennerberg, *et al.*, Effects of titanium surface topography on bone integration: a systematic review, *Clin. Oral Implants Res.*, 2009, **20**(Suppl 4), 172–184.
48 R. A. Gittens, *et al.*, Implant osseointegration and the role of microroughness and nanostructures: Lessons for spine implants, *Acta Biomater.*, 2014, **10**(8), 3363–3371.
49 S. A. Goldstein, The mechanical-properties of trabecular bone - dependence on anatomic location and function, *J. Biomechanics*, 1987, **20**(11–12), 1055–1061.
50 L. Gibson, *et al.*, *Cellular solids: structure and properties*, 2nd edn, Cambridge University Press, Cambridge, 1997.
51 A. Petersen, *et al.*, A biomaterial with a channel-like pore architecture induces endochondral healing of bone defects, *Nat. Commun.*, 2018, **9**(1), 4430.
52 J. W. Milgram, Nonunion and pseudarthrosis of fracture healing. A histopathologic study of 95 human specimens, *Clin. Orthop. Relat. Res.*, 1991, **268**, 203–213.
53 D. H. Carter, *et al.*, Immunolocalization of collagen types I and III, tenascin, and fibronectin in intramembranous bone, *J. Histochem. Cytochem.*, 1991, **39**(5), 599–606.
54 R. Z. LeGeros, Properties of osteoconductive biomaterials: Calcium phosphates, *Clin. Orthop. Rel. Res.*, 2002, **395**, 81–98.
55 A. A. C. Reed, *et al.*, Human atrophic fracture non-unions are not avascular, *J. Orthop. Res.*, 2002, **20**(3), 593–599.
56 J. M. Anderson, *et al.*, Foreign body reaction to biomaterials, *Semin. Immunol.*, 2008, **20**(2), 86–100.
57 H. K. Väänänen, *et al.*, Osteoclast lineage and function, *Arch. Biochem. Biophys.*, 2008, **473**(2), 132–138.
58 S. Wenisch, *et al.*, In vivo mechanisms of hydroxyapatite ceramic degradation by osteoclasts: fine structural microscopy, *J. Biomed. Mater. Res. A*, 2003, **67**(3), 713–718.
59 F. Loi, *et al.*, Inflammation, fracture and bone repair, *Bone*, 2016, **86**, 119–130.
60 G. S. Baht, *et al.*, The Role of the Immune Cells in Fracture Healing, *Curr. Osteoporos. Rep.*, 2018, **16**(2), 138–145.
61 T. Iwakura, *et al.*, Human hypertrophic nonunion tissue contains mesenchymal progenitor cells with multilineage capacity in vitro, *J. Orthop. Res.*, 2009, **27**(2), 208–215.
62 S. Bajada, *et al.*, Decreased osteogenesis, increased cell senescence and elevated Dickkopf-1 secretion in human fracture non union stromal cells, *Bone*, 2009, **45**(4), 726–735.

